Modeling the transition of the inner plasma sheet from weak to enhanced convection

Chih-Ping Wang and Larry R. Lyons
Department of Atmospheric and Oceanic Sciences, University of California, Los Angeles, California, USA

Margaret W. Chen
Space Science Applications Laboratory, The Aerospace Corporation, El Segundo, California, USA

Frank R. Toffoletto
Department of Physics and Astronomy, Rice University, Houston, Texas, USA

Received 18 May 2004; revised 18 August 2004; accepted 2 September 2004; published 2 December 2004.

[1] We seek to determine whether the adiabatic plasma transport and energization resulting from electric and magnetic drift can quantitatively account for the plasma sheet under weak and enhanced convection observed by Geotail presented in the companion paper [*Wang et al.*, 2004]. We use a modified Magnetospheric Specification Model to simulate the dynamics and distributions of protons originating from the deep tail and low-latitude boundary layer (LLBL) under an assigned, slowly increasing convection electric field. The magnetic field is Tsyganenko 96 model, modified so that force balance is maintained along the midnight meridian. Our simulation results reproduce well the observed radial profiles and magnitudes of pressure and magnetic field. The changes of these parameters with convection strength are also well reproduced, indicating that the electric and magnetic drift control the large-scale structure of the plasma sheet. The plasma flows near midnight are diverted toward dusk by diamagnetic drift. We obtain a steady state plasma sheet under strong and steady convection, showing that magnetic drift and field line stretching bring the plasma sheet away from possible convection disruption. The protons from the LLBL strongly affect the plasma sheet density and temperature during quiet times but not during enhanced convection. For the same cross–polar cap potential, stronger shielding of the convection electric field results in smaller energization. The penetration electric field is important in moving the plasma sheet to smaller geocentric radial distance. Our results suggest that the frozen-in condition $\mathbf{E} = -\mathbf{v} \times \mathbf{B}$ is not valid in the inner plasma sheet because of strong diamagnetic drift. *INDEX TERMS:* 2764 Magnetospheric Physics: Plasma sheet; 2753 Magnetospheric Physics: Numerical modeling; 2760 Magnetospheric Physics: Plasma convection; 2740 Magnetospheric Physics: Magnetospheric configuration and dynamics; 2744 Magnetospheric Physics: Magnetotail; *KEYWORDS:* inner plasma sheet, Magnetospheric Specification Model, weak convection, enhanced convection, plasma moments, magnetic field

Citation: Wang, C.-P., L. R. Lyons, M. W. Chen, and F. R. Toffoletto (2004), Modeling the transition of the inner plasma sheet from weak to enhanced convection, *J. Geophys. Res.*, *109*, A12202, doi:10.1029/2004JA010591.

1. Introduction

[2] The convection electric field resulting from the coupling of the Earth's magnetosphere with the solar wind drives plasma in the tail plasma sheet earthward. This transport results in plasma heating and magnetic field stretching, which becomes very significant in the inner plasma sheet. (The inner plasma sheet in this paper refers to the region of the plasma sheet between its earthward edge and $X_{GSM} \sim -20\ R_E$. The earthward edge of the plasma sheet is located at $X_{GSM} \sim -10\ R_E$ at midnight during quiet times. Its location moves earthward as the convection electric field increases and can move to $X_{GSM} > -5\ R_E$ during storm times). The stored energy and the transport itself are important sources for geomagnetic disturbances. For example, the spatial distribution of enhanced plasma energy is important for understanding current wedge formation and auroral breakup during substorms [e.g., *Samson et al.*, 1992], and the inward motion of the plasma sheet during storms is important for the formation of the storm time ring current [e.g., *Chen et al.*, 1994; *Kozyra et al.*, 1998]. Therefore it is crucial to examine if the plasma transport and energization driven by convection can result in the plasma sheet distributions responsible for storms, substorms, and other geomagnetic disturbances.

[3] Previous models and simulations are able to qualitatively explain some plasma sheet observations [e.g., *Spence*

0148-0227/04/2004JA010591$09.00

and Kivelson, 1993; *Ashour-Abdalla et al.*, 1994; *Ogino et al.*, 1992; *Walker et al.*, 1993]. However, due to the difficulty in numerical computations most simulations neglect some of the physical processes that can be important in the plasma sheet dynamics, which weakens their validity in making quantitative comparisons with observations. For example, the frozen-in condition, which is used in ideal MHD, is not valid in the plasma sheet due to strong diamagnetic drift [*Hori et al.*, 2000; *Wang et al.*, 2003] and in test particle simulations the effect of magnetic field changes due to particle currents is not fully taken into account. As a result, even the basic structures of the plasma sheet revealed from numerous measurements of plasma moments and magnetic fields [e.g., *Huang and Frank*, 1986, 1994a, 1994b; *Baumjohann et al.*, 1989; *Spence et al.*, 1989; *Kistler et al.*, 1993; *Wing and Newell*, 1998] still have not yet been quantitatively compared with simulations. A long-standing question concerning the existence of force-balanced plasma sheet solution for constant convection [*Erickson and Wolf*, 1980] has been answered qualitatively by simulations [*Hau et al.*, 1989; *Hau*, 1991; *Erickson*, 1992], but the question of stability has not been adequately addressed and the issue is, in any case, not resolved without support from quantitative agreement with observations.

[4] The objective of our study is to model the inner plasma sheet by taking into account the major large-scale processes affecting the plasma and fields, including major plasma sources. We developed a modified version of the Magnetospheric Specification Model [*Freeman et al.*, 1993] and combined it with a modified version of the Tsyganenko 96 model [*Tsyganenko*, 1995, 1996] to model electric and magnetic drift of protons. The model assumes particles come from model boundary particle sources that are a mixture of particles from the deep tail and from the low-latitude boundary layer (LLBL). Two-dimensional force balance is maintained along the midnight meridian. We previously used this model to simulate the plasma sheet under weak convection [*Wang et al.*, 2001, 2002] and the results reproduced quantitatively the general features of the quiet time plasma sheet. We also investigated the evolution of the plasma sheet under a condition of increasing cross polar cap potential drop but with the convection electric field strongly shielded at $r \sim 10\ R_E$ [*Wang et al.*, 2003]. The shielding prevented the plasma from getting into regions of strong magnetic field even when the potential drop is high. As a result, the simulated pressure could account for the observed pressure increase from low to moderate activity but underestimated the increase by a factor of 2 from low to high activity.

[5] The focus of the present work is to simulate the earthward penetration of the plasma sheet under enhanced convection by taking into account more realistic shielding effects as the potential drop increases. This allows us to evaluate quantitatively whether the transport and energization associated with electric and magnetic drifts are indeed sufficient to account for the Geotail observations for quiet times (weak convection) and the substorm growth phase (enhanced convection) that we have analyzed in the companion paper [*Wang et al.*, 2004] (hereinafter referred to as Paper 1). We also investigate if the earthward penetration can explain observed changes at geosynchronous orbits. We present in this paper the simulation results and their comparisons with the observations, and discuss the importance of shielding of the convection electric field, the penetration electric field, and diamagnetic drift.

2. Modeling and Simulation Description

[6] In this simulation only protons are modeled. Electrons are neglected since their pressure is typically an order of magnitude lower than the proton pressure [*Spence et al.*, 1989]. Other ion species are also neglected because of their low concentration compared to protons. Even though O^+ ions are very important for the storm time ring current, their access to the plasma sheet as a function of local time and radial distance is still not well understood. Therefore we don't explore the O^+ contribution in this simulation. We simulate the plasma transport and energization by large-scale plasma drift; transport associated with bursty flows and substorm injections during the expansion phase are not included. In this section we briefly describe the models and the conditions used in this simulation.

2.1. Magnetospheric Specification Model

[7] The Magnetospheric Specification Model (MSM) [*Freeman et al.*, 1993] calculates the bounce–averaged electric drift and magnetic drift of a flux tube filled with an isotropic distribution of ions or electrons with a set of specified kinetic energies within the closed field line region of the magnetosphere. Assuming that the particle distributions are isotropic and that the drift motion is adiabatic, the change in the particle kinetic energy can be determined from the change of flux tube volume along its drift path according to the relation [*Wolf*, 1983]

$$E_k = \lambda V^{-2/3}, \tag{1}$$

where E_k is the particle's kinetic energy, λ is constant along a particle's drift path and is called the energy invariant, and V is the flux tube volume per unit magnetic flux that is defined as $V = \int ds/B$, where B is the magnitude of the magnetic field and ds is the differential unit element along the field line. The bounce-averaged drift $\mathbf{v}_D$ at position $\mathbf{x}$ and time t is independent of pitch angle and can be described as [*Wolf*, 1983]

$$\mathbf{v}_D(\mathbf{x},t) = \frac{\mathbf{B}(\mathbf{x},t) \times \nabla\left(\Phi(\mathbf{x},t) + \lambda V(\mathbf{x},t)^{-2/3}/q\right)}{|\mathbf{B}(\mathbf{x},t)|^2}, \tag{2}$$

where Φ is the electric potential in a frame that rotates with the Earth, $\mathbf{B}$ is the magnetic field, and q is the particle's electric charge. The first term on the right side of (2) is the electric drift and the second term is the magnetic drift. The assumptions used in deriving (2) are valid in the plasma sheet and detailed discussions are given by *Wang et al.* [2001, 2003]. Using an electric and a magnetic field model to provide $\Phi(\mathbf{x}, t)$ and $V(\mathbf{x}, t)$, the drift trajectory of particles of a given energy invariant λ within a flux tube is traced using (2) in the MSM.

[8] With particle distributions specified inside the model as an initial condition and along the model boundary as particle sources, the subsequent evolution of the particle distributions resulting from the different drifts of different

energy protons are then calculated. Details about the region of our modified MSM and how the MSM simulates particle fluxes and distributions of plasma pressure, number density, and temperature are given by *Wang et al.* [2001].

2.2. Electric and Magnetic Field Models

[9] The MSM calculates the bounce-averaged drift velocity (2) in the ionosphere. Therefore $\mathbf{B}(\mathbf{x}, t)$ and $\Phi(\mathbf{x}, t)$ in (2) are the Earth's dipole field and the electric potential in the ionosphere. The drift due to induction electric field is negligible in the ionosphere. The convection electric field used in our model is essentially that of the original MSM, which has been developed to represent a realistic convection electric field. The modeled distribution of the electric field potential inside the polar cap is based on the Heppner and Maynard empirical model [*Heppner and Maynard*, 1987] and the potential at low latitudes (equatorward of the auroral latitudes) is based on the Rice Convection Model [*Spiro et al.*, 1988]. At auroral latitudes the electric potential is an analytic formula that gives conventional sunward convection and joins smoothly with the formula used at higher and lower latitudes. The electric field is shielded at low latitudes and the change of shielding latitude with activity is modeled based on the observed equatorward edge of the diffuse aurora [*Gussenhoven et al.*, 1983]. The model also allows the convection electric field to penetrate to latitudes lower than the shielding latitude when there is time change in the cross polar cap potential drop ($\Delta\Phi_{PC}$). The electric field model is controlled by parameters that include the size of the polar cap, an interplanetary magnetic field (IMF)-dependent convection pattern inside the polar cap, $\Delta\Phi_{PC}$, the latitude of the shielding layer, and the penetration electric field. Except for $\Delta\Phi_{PC}$, all these parameters are controlled by a single input Kp in the original MSM.

[10] A magnetic field model is used to calculate $V(\mathbf{x}, t)$ and to map plasma distributions from the ionosphere to the equatorial plane. If the model magnetic fields are self-consistent with the plasma pressure, then the distributions mapped to the equatorial plane are results of equatorial plasma motion that includes induced electric fields. To obtain a force balanced magnetic field, we have developed a modified version of the Tsyganenko 96 (T96) magnetic field model by adding a set of additional, adjustable small-scale circular current loops [*Tsyganenko*, 1998] to a magnetic field configuration generated by the original T96 model. Descriptions of the adjustable current loops and how they are incorporated into the original T96 are given by *Wang et al.* [2002]. With this flexibility, we adjust the amplitude and direction of the additional current loops and their associated shielding magnetic field in the modified T96 to maintain $(\mathbf{j} \times \mathbf{B})_x = (\nabla p)_x$ and $\int_0^{15\,R_E} (\mathbf{j} \times \mathbf{B})_z dz' = p(z = 0)$ along the midnight plane in the region of the plasma sheet. Because of large computing time associated with the use of the small-scale adjustable current, we adjust the currents till the maximum error in the force balance requirements is $\leq$20%. Even though we only maintain force balance along the midnight meridian, due to the use of the circular loops there is still approximate force balance inside $|Y_{GSM}| \sim 5\ R_E$. The force balance gradually worsens toward larger $|Y_{GSM}|$ where ∇p in the y direction becomes important, which occurs especially near the inner edge of the plasma sheet.

2.3. Initial and Boundary Particle Sources

[11] The initial particle flux is generated in the MSM by fitting kappa or bi-kappa distributions to Kp-sorted observations at L = 3, 4, 6.6, and 13 and then interpolating to every grid inside the model region. The initial distribution is not important to the simulated plasma sheet populations, which consists of particles drifting along open trajectories from the particle sources at the model boundary. However, it is necessary to include initial conditions in our simulation in order to obtain a continuous pressure profile from the plasma sheet to the inner magnetosphere so force balance can be checked at the inner edge of the plasma sheet.

[12] The boundary particle distributions take into account warmer particles that originate from the mantle and are transported earthward from the distant tail to our model outer boundary and cooler particles from the low-latitude boundary layer (LLBL). The mixing of these two populations is described by a bi-kappa particle distribution (a sum of two kappa distributions):

$$f = N_1 \left(\frac{m}{2\pi\kappa_1 E_{0,1}}\right)^{3/2} \frac{\Gamma(\kappa_1 + 1)}{\Gamma(\kappa_1 - 1/2)} \left[1 + \frac{E}{\kappa_1 E_{0,1}}\right]^{-\kappa_1 - 1} + N_2 \left(\frac{m}{2\pi\kappa_2 E_{0,2}}\right)^{3/2} \frac{\Gamma(\kappa_2 + 1)}{\Gamma(\kappa_2 - 1/2)} \left[1 + \frac{E}{\kappa_2 E_{0,2}}\right]^{-\kappa_2 - 1}, \quad (3)$$

where N is the densities, m is particle mass, E_0 is the energy of the peak particle flux, and κ is constant. The warmer (cooler) population is determined by parameters with subscript 1 (2) and will be referred to as the tail (LLBL) source in this paper. The values of N, κ, and E vary with local time. We used observations from Geotail [*Paterson et al.*, 1998] and the results of the finite-tail-width convection model [*Spence and Kivelson*, 1993] as guidelines to construct the boundary particle fluxes at different local times. The locations of the model boundary in the equatorial plane and values of Es and Ns are given in Table 1 of *Wang et al.* [2001].

2.4. Conditions for the Simulation

[13] The goal of the current study is to understand how the plasma sheet varies quantitatively from weak to strong convection electric field. Therefore we single out two major parameters, $\Delta\Phi_{pc}$ and the shielding latitude (θ) in the electric field model to control the change of convection strength. θ is a function of Kp in the original MSM and in this simulation a conversion $\Delta\Phi_{pc}$ = 14.587 kV + 17 kV·Kp is used to obtain θ as a function of $\Delta\Phi_{pc}$. We use a constant polar cap size corresponding to Kp = 1 and a convection pattern for IMF $B_y = 0$, and IMF $B_z < 0$.

[14] The $\Delta\Phi_{pc}$ and θ used in this simulation are shown in Figure 1a. We first run our simulation under a condition of weak convection ($\Delta\Phi_{pc}$ = 26 kV and θ = 66.5°) for 10 hours till quiet time equilibrium is reached. Beginning at $t = 0$, we gradually and steadily increase the convection strength by increasing $\Delta\Phi_{pc}$ to 146 kV and decreasing θ to 51.8° at t = 300 min. The increasing $\Delta\Phi_{pc}$ with time would have resulted in a penetration electric field. Since our focus of this simulation is to study the average behavior of the inner plasma sheet corresponding to different strength of $\Delta\Phi_{pc}$,

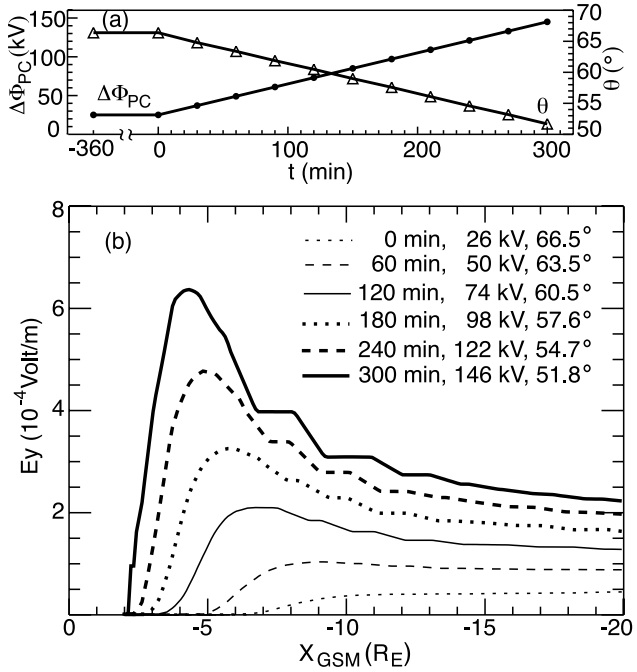

Figure 1. (a) Assigned $\Delta\Phi_{pc}$ (dot) and θ (triangle) as a function of time. (b) The *y* component of convection electric field at midnight in the equatorial plane for different assigned convection strengths.

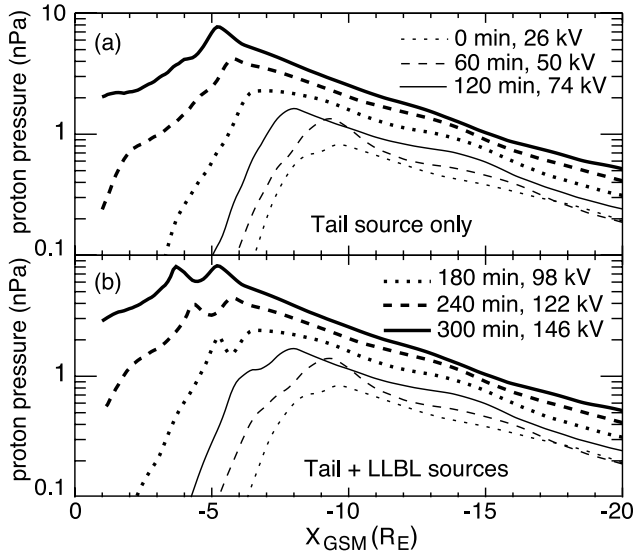

Figure 2. Radial profiles of the simulated pressure of protons from (a) the tail source only and from (b) both the tail and LLBL sources in the equatorial plane averaged over $|Y_{GSM}| \leq 5\ R_E$.

we deliberately set the penetration electric field to be zero so the inner edge of the plasma sheet is determined only by θ. To study the plasma sheet under constant convection, we also run the simulation under two different levels of constant convection corresponding to constant $\Delta\Phi_{PC}$ = 98 kV (146 kV) and θ = 57.6° (51.8°) after t = 180 (300 min). Throughout the simulations, the boundary particle sources are kept time-independent.

[15] We choose the parameters P_{SW} (solar wind dynamic pressure) = 1 nPa, Dst = −10 nT, IMF B_y = 0, and IMF B_z = 5 nT and no dipole tilt for the original T96 magnetic field, to which we add the additional, adjustable small-scale circular current loops. We do not change the T96 parameters during the simulation.

[16] A change in convection strength inside the magnetosphere or solar wind dynamic pressure result in pressure changes in both the plasma sheet and the lobes in maintaining force balance within the magnetosphere, as well as changes in the location and flaring angle of the magnetopause in maintaining force balance between the magnetosphere and solar wind. However, the magnetopause used in the Tsyganenko 96 model is determined solely by P_{SW}, and we used a fixed P_{SW} value to exclude the effects of varying dynamic pressure. This prevents us from taking into account the effects of magnetopause flaring angle changes. Therefore our simulation results show the self-consistent evolution of the plasma sheet and the lobes under enhanced convection confined inside a fixed magnetopause.

[17] Figure 1b shows the *y* component of the convection electric field at midnight in the equatorial plane, which is obtained by mapping the convection electric potential determined by $\Delta\Phi_{pc}$ and θ shown in Figure 1a to the equatorial plane using the force balanced magnetic field.

3. Simulation Results

[18] In this section we present and discuss the results of the simulation for different levels of convection strength. The results are compared with the observations shown in Paper 1 to determine whether our calculations can account

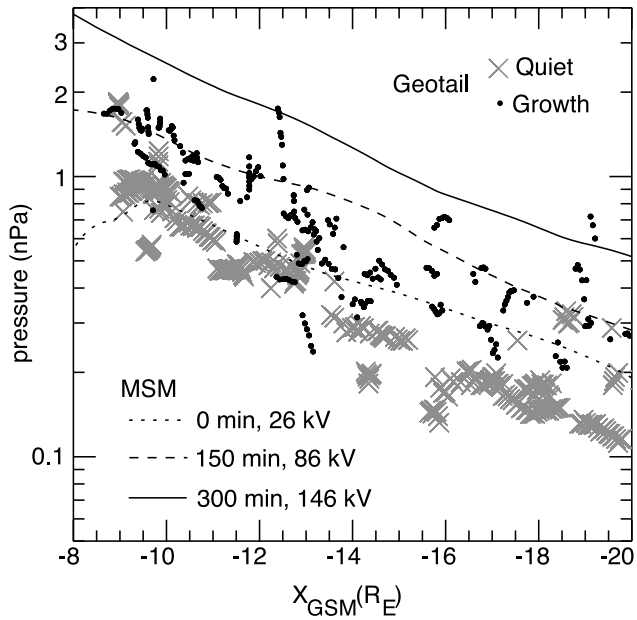

Figure 3. Comparisons between the simulated proton pressures shown in Figure 2b and the Geotail total pressures shown in Figures 2d and 2e in Paper 1.

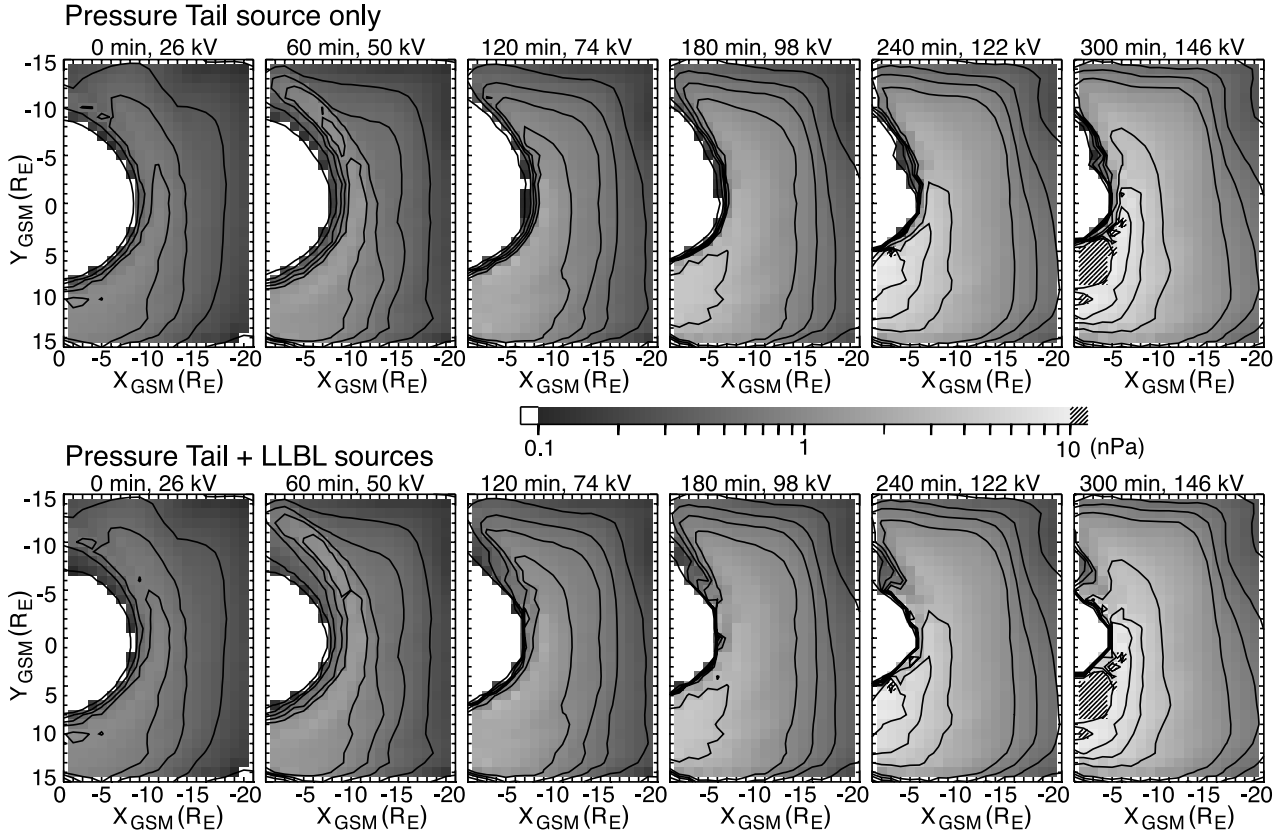

Figure 4. Simulated pressure of protons from (top) tail source only and from (bottom) both the tail and LLBL sources in the equatorial plane. See color version of this figure in the HTML.

for the observed changes in the plasma sheet from weak to strong convection.

3.1. Proton Pressure

[19] As convection increases, the inward edge of the convection electric field in the equatorial plane at midnight, as shown in Figure 1b, moves earthward from ~10 R_E for $\Delta\Phi_{PC}$ = 26 kV to ~4 R_E for $\Delta\Phi_{PC}$ = 146 kV. Figure 2a shows the radial profiles of the simulated total pressure of protons from the tail source only in the equatorial plane for different $\Delta\Phi_{PC}$ averaged over $|Y_{GSM}| \leq 5\ R_E$. In Figures 2–8 we do not include the contribution of protons from the initial conditions to proton pressure, number density, and temperature. This effectively removes the contributions from particles on closed drift trajectories, and thus emphasizes the locations of the inner edge of the plasma sheet, which result from particles on open drift trajectories. Regardless of convection strength, the proton pressure increases with decreasing distance from the Earth, reaching a peak at ~1 R_E tailward of the earthward edge of the convection electric field. Figure 2b shows the simulated pressures including both the tail and LLBL sources and the comparison with Figure 2a shows that particles from the tail source are responsible for essentially all the pressure throughout most of the plasma sheet.

[20] In addition to the large pressure increases at $r < 10\ R_E$ resulting from the earthward penetration motion of the inner edge of the plasma sheet as convection increases, the pressures increase everywhere else in the plasma sheet with increasing $\Delta\Phi_{PC}$, the enhancement being slightly stronger at smaller radial distance. The overall pressure between X_{GSM} = −10 to −20 R_E increases by a factor of ~1.7 as $\Delta\Phi_{PC}$ increases from 0 to 86 kV and a factor of ~2.9 from 0 to 146 kV. This is better than the results of our previous simulation, where we did not allow the plasma sheet to move earthward [*Wang et al.*, 2003], and it is in better agreement with previously published observations shown in Table 1 of *Wang et al.* [2003]. The effect of the shielding on plasma sheet energization is further discussed in section 4.1. Figure 3 shows comparisons between the Geotail total pressures (ion plus magnetic pressure) in the lobes shown in Figure 2 in Paper 1 and our simulated proton pressures in the equatorial plane shown in Figure 2b. As discussed in Paper 1, during quiet times the Geotail lobe total pressure is almost the same as the plasma sheet total pressure. However, during the growth phase due to the effects that total pressure continually increases and Geotail often moved from the central plasma sheet to the lobes as field lines become more stretched, the Geotail total pressure in lobes is better than the Geotail total pressure in the central plasma sheet in representing the true growth phase ion pressure in the equatorial plane. Our pressures for $\Delta\Phi_{PC}$ = 26 kV in general reproduces well the observed pressure during quiet times, though the modeled pressures are slightly higher than most of the measurements at large radial distance. The majority of the observed pressures during the substorm growth phase fall between our pressures for $\Delta\Phi_{PC}$ = 26 and 86 kV. This range of $\Delta\Phi_{PC}$ is typical of those observed during the

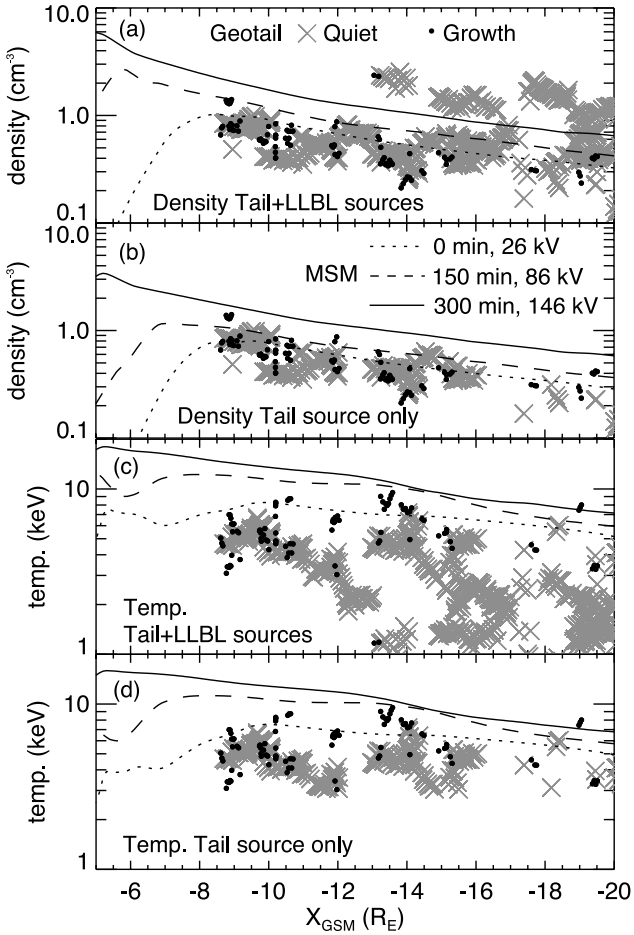

Figure 5. (a) Radial profiles of the simulated number density of protons from both the tail and LLBL sources in the equatorial plane averaged over $|Y_{GSM}| \leq 5\ R_E$ compared with the Geotail density. (b) Comparison between the Geotail density (only measurements with temperature higher than 3 keV) and simulated number density of protons from the tail source only. (c) Radial profiles of the simulated temperature of protons from both the tail and LLBL sources in the equatorial plane averaged over $|Y_{GSM}| \leq 5\ R_E$ compared with the Geotail temperature. (d) Comparison between the Geotail temperature (only measurements with temperature higher than 3 keV) and simulated temperature of protons from the tail source only.

growth phase of substorms [*Weimer et al.*, 1992], so that we expect most observations to fall within this range of pressures for these values of $\Delta\Phi_{PC}$. Our modeled pressure for $\Delta\Phi_{PC}$ = 146 kV approximately marks the upper limit of the observed pressures during the growth phase, which is reasonable since 146 kV is significantly larger than typical growth phase values but is still a value that is occasionally attainable. In addition, at geosynchronous orbit near midnight our simulated proton pressure for $\Delta\Phi_{PC} = 86$ kV is also very close to the average observed proton pressure ($\sim$1.4 nPa for Kp = 3) reported by *Korth et al.* [1999]. These good agreements show that the energization associated with large-scale drift can account for the plasma sheet pressure increase when convection is enhanced.

[21] The top panels of Figure 4 show the distributions of the simulated pressure of protons within the equatorial plane from the tail source only. The pressure profile for weak convection is seen to be relatively uniform across the tail at larger radial distance, but to have a weak dawn-dusk asymmetry at smaller radial distance with higher pressure on the dusk side. The asymmetry results from the duskward magnetic drift of protons in the plasma sheet and is most significant at the inner edge of the plasma sheet. As convection increases, the whole plasma sheet moves earthward and the asymmetry at the inner edge intensifies. The bottom panels of Figure 4 show the simulated proton pressures including both the tail and LLBL sources. Comparing with the top panels of Figure 4 shows that the protons from the LLBL have little contribution to pressure throughout the plasma sheet except in the postmidnight sector inside $r \sim 10\ R_E$ during strong convection.

[22] In general, the trends of the simulated 2-D pressure distributions with increasing $\Delta\Phi_{pc}$ agree well with the trends seen in the DMSP observations from quiet to high activity levels [see *Wing and Newell*, 1998, Plate 1]. The equatorial DMSP profiles are obtained by mapping the observations from the low altitude. The strong dawn-dusk asymmetry during strong convection shown in our results is likely stronger than it should be since we do not maintain force balance in the y direction in our simulation. More realistic field lines on the dusk (dawn) side should be more (less) stretched than our magnetic fields, therefore yielding lower (higher) pressure on the dusk (dawn) side than our pressures.

3.2. Proton Number Density and Temperature

[23] The simulated densities and temperatures averaged over $|Y_{GSM}| \leq 5\ R_E$ including both the tail and LLBL sources for three different levels of $\Delta\Phi_{PC}$ are plotted in Figures 5a and 5c, respectively and are compared with the Geotail data for the quiet and growth conditions. Both the simulated density and temperature, for all $\Delta\Phi_{pc}$, increase with decreasing radial distance from the Earth but the radial gradients of temperature appear to be smaller than the gradients of pressure and density. The overall magnitude of density (temperature) between $X_{GSM} = -10$ to $-20\ R_E$ increases by a factor of $\sim$1.3 (1.2) as $\Delta\Phi_{PC}$ increases from 0 to 86 kV and a factor of $\sim$2 (1.46) from 0 to 146 kV. However, the Geotail data shows that density is often higher during quiet times than during the growth phase. This is likely due to the LLBL source being much stronger during quiet times than during disturbed times [*Mitchell et al.*, 1987; *Miura*, 1995; *Fujimoto et al.*, 1998], so that mixing of the denser and colder particles from the LLBL with the particles from the tail results in higher density and lower temperature. As discussed in Paper 1, the quiet time ions observed by Geotail, as can be seen in Figures 5a and 5c, are at times very cold and dense indicating that the ion population is dominated by ions from the LLBL, while at other times the observed ions are warmer and less dense indicating that the population is dominated by ions from the tail. In Paper 1 we used an arbitrary, radial distance–independent 3 keV temperature discriminator to approximately separate these two populations.

[24] We plot the simulated densities and temperatures of protons from the tail source only in Figures 5b and 5d

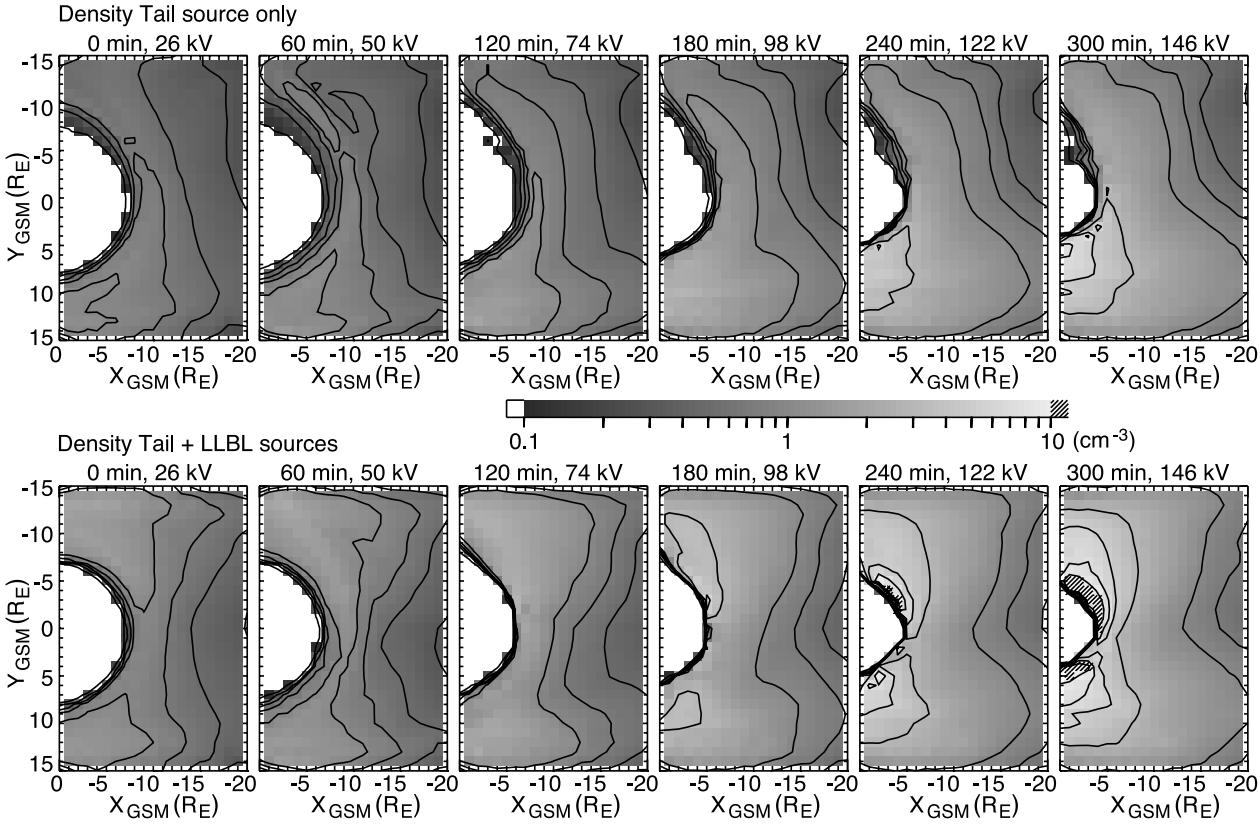

Figure 6. Simulated number density of protons from (top) the tail source only and from (bottom) both the tail and LLBL sources in the equatorial plane. See color version of this figure in the HTML.

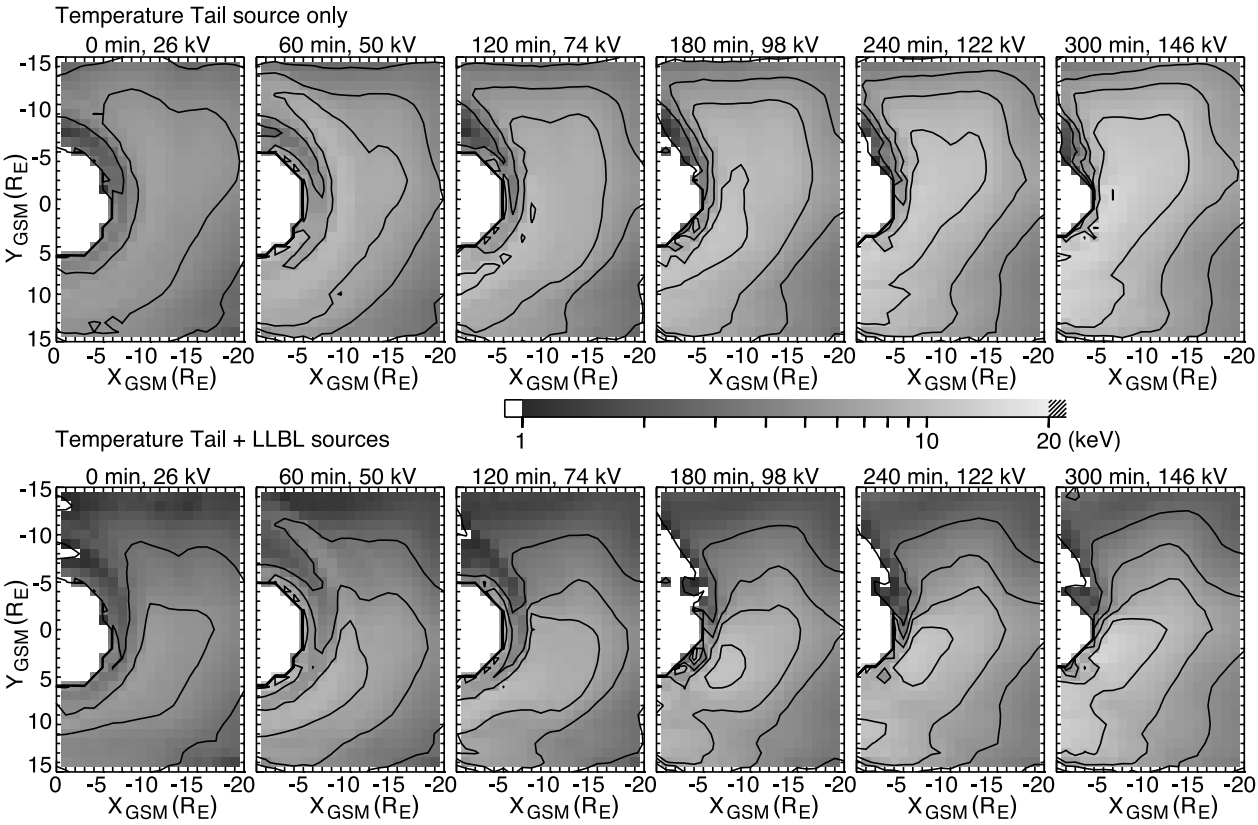

Figure 7. Simulated temperature of protons from (top) the tail source only and from (bottom) both the tail and LLBL sources in the equatorial plane. See color version of this figure in the HTML.

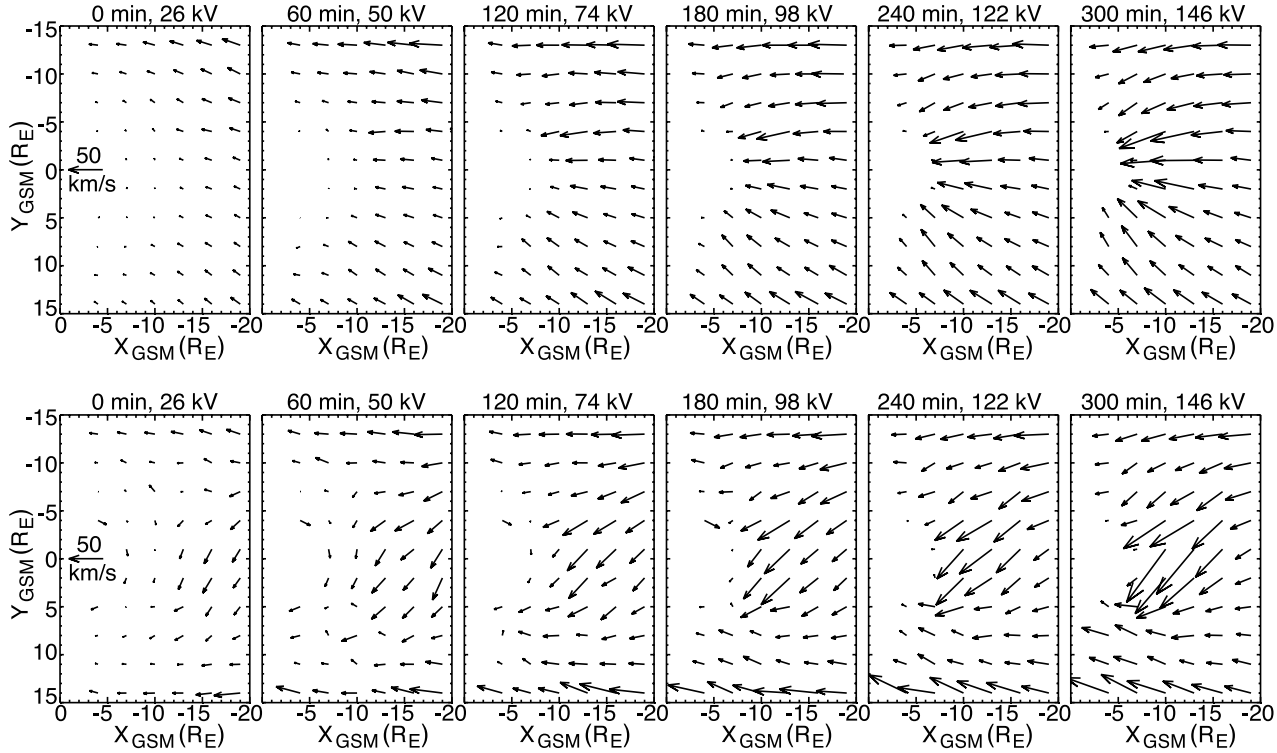

Figure 8. (top) Simulated electric drift and (bottom) proton's total drift (electric plus diamagnetic drift) in the equatorial plane.

respectively and compare with the Geotail data for cases with T > 3 keV, which are presumably for times when the population is dominated by ions from the tail. For quiet times we see in Figures 5b and 5d that the simulated densities and temperatures go through most of the Geotail data, which indicates that our model gives realistic quiet time densities and temperatures at times when the LLBL particles do not have access to, or have not yet accessed, the near-midnight region. However, when the LLBL source is included as shown in Figures 5a and 5c, the simulated densities and temperatures cannot account for the high-density and low-temperature Geotail data points, which are presumably for times dominated by LLBL ions. This indicates that our model LLBL source underestimates the realistic particle supply from the quiet time LLBL. For the growth phase, unlike for quiet times, Geotail observed almost no cases with very high ion density and low temperature, and we find that, for most of the growth phase, Geotail data points are just below our profiles for $\Delta\Phi_{PC}$ = 86 kV with or without the LLBL contribution. The agreement is somewhat better without the LLBL source. This result suggests that there is very little LLBL contribution to the plasma sheet ion population near midnight during times of strong convection.

[25] *Borovsky et al.* [1997] showed that the majority of the plasma densities observed at the midnight geosynchronous orbit lie roughly between 0.4–1.2 cm^{-3} when the solar wind dynamics pressure is less than 10 nPa. *Korth et al.* [1999] reported that the proton density (temperature) at the same location is ~0.75 cm^{-3} (8.5 keV) for Kp = 3. These observations are in reasonable agreement with our density (~1 cm^{-3}) and temperatures (~10 keV) for $\Delta\Phi_{PC}$ = 86 kV without the LLBL contribution.

[26] The top panels of Figures 6 and 7 show the simulated proton densities and temperatures respectively within the equatorial plane for different $\Delta\Phi_{PC}$ including the tail source only. For weak convection, protons from the tail drift duskward as they move earthward, which results in higher density and temperature in the premidnight region. As convection increases, stronger electric drift allows high-energy particles from the dawnside model boundary to penetrate further earthward in the postmidnight sector before they drift toward the dusk side, resulting in an increase of density and temperature throughout the plasma sheet in both pre and postmidnight sectors and higher density and temperature at premidnight near the inner edge of the plasma sheet. On the other hand, protons from the LLBL source, because they are cold and thus dominated by electric drift, flow mainly earthward after entering the magnetosphere from the flanks. This results in regions of high density and low temperature near the two flanks as seen in the bottom panels of Figures 6 and 7, which show results including both the tail and LLBL sources. These profiles for weak convection in general agree with the DMSP profiles [*Wing and Newell*, 1998]. However, during strong convection our profiles without the LLBL source have better agreement with the DMSP profiles, indicating the access of the LLBL particles into the magnetosphere becomes ineffective during strong convection.

3.3. Proton Flow

[27] The average total drift velocity $\langle \mathbf{v} \rangle$ of isotropic protons is

$$\langle \mathbf{v} \rangle = \frac{\mathbf{B} \times \nabla \mathbf{F}}{B^2} + \frac{\mathbf{B} \times \nabla p}{neB^2}, \quad (4)$$

where n is number density and e is the electron charge. The first term on the right-hand side of (4) is the electric drift and the second term is the diamagnetic drift, which is the sum of magnetic drift and the magnetization effect.

[28] The calculated proton electric drift (including convection, induced, and corotation electric drift) in the equatorial plane for different $\Delta\Phi_{PC}$ are shown in the top panels of Figure 8 and total drifts are shown in the bottom panels. The electric drift is mainly directed toward the Earth and its magnitude is relatively constant across the tail due to the relatively uniform duskward convection electric field across the tail generated by the MSM. The diamagnetic drift for protons is mainly directed azimuthally toward positive Y_{GSM}. For quiet times the flow near the dawn flank of the plasma sheet is dominated by electric drift. Since proton's number density in this region is relatively high (see Figure 6) and their temperature is relatively low (see Figure 7), their diamagnetic drift is small. Because the number density decreases and the pressure increases from the dawn flank toward midnight, the component of diamagnetic drift gradually becomes stronger from the dawn flank to midnight and eventually becomes as important as the electric drift. As a result, the flows are gradually diverted toward the dusk side as the diamagnetic drift grows. The diamagnetic drift dominates the premidnight flow. It then gradually decreases in magnitude toward the dusk flank due to the larger number density along the dusk flank and becomes smaller than the magnitude of electric drift. Therefore this flow pattern shows that the plasma transported earthward from the distant tail is mainly diverted toward dusk in the inner plasma sheet and only plasma near the dawn flank maintains its earthward motion. The asymmetry in the flow indicates that the cool protons on the dawn side continue their motion to the dayside magnetopause but part of the hot proton population on the dusk side may be lost across the dusk magnetopause because of azimuthal drift.

[29] As $\Delta\Phi_{PC}$ increases, we can see in Figure 8 that the overall flow speed increases but the flow directions have no significant changes. This indicates that both the electric drift and diamagnetic drift are enhanced as a result of an increased convection electric field. An important feature in our simulation results is that flows near midnight are strongly diverted toward dusk by diamagnetic drift. Such flows are similar to the Geotail flows for quiet and growth phase periods shown in Figure 8 of Paper 1, the quiet time flow observed by AMPTE and ISEE [*Angelopoulos et al.*, 1993; *Angelopoulos*, 1996], and the flows averaged over all levels of activity measured by Geotail [*Hori et al.*, 2000]. The increase of flow speed with enhanced convection is also seen in the Geotail flows in Paper 1 and the ISEE flows reported by *Zhu* [1993]. Our flow speed between $-10\ R_E \geq X_{GSM} \geq -20\ R_E$ and $|Y_{GSM}| \leq 5\ R_E$ increases from $\sim$20 km/s for $\Delta\Phi_{PC}$ = 26 to $\sim$35 km/s for 86 kV, an increase similar to the increase in the Geotail speed in the same region shown in Paper 1. However, there are some differences between the simulated flows and the Geotail flows shown in Paper 1. Comparison between the simulated flows and the Geotail flows shown in Figure 8 in Paper 1 shows that in the region $0 \geq Y_{GSM} \geq -5\ R_E$, for both weak and strong convection, the simulated V_y agrees well with the Geotail perpendicular V_y. However, the simulated V_x increases with enhanced convection while the Geotail V_x remains nearly zero. On the other hand, in the region $5\ R_E \geq Y_{GSM} \geq 0$, for both weak and strong convection, the simulated V_x, is in good agreement with the Geotail V_x, but the simulated V_y is about a factor of 2 smaller than the Geotail V_y. Therefore the Geotail flows appear to have stronger duskward drift than our simulated flows in both quiet and enhanced convection conditions. However, there are two effects that can explain the differences. As we discussed in Paper 1, due to the magnetic field's elevation angle, the Geotail perpendicular V_x can be smaller than it would be at the center of the current sheet. In addition, we increased convection very slowly in our simulation, resulting in slow magnetic field stretching. This gives small induced electric drift (induced $V_x \sim -10$ to -15 km/s at midnight in the region $-10\ R_E \geq X_{GSM} \geq -20\ R_E$ when $\Delta\Phi_{PC}$ increases from 74 to 86 kV) associated with the field line stretching. Many of the growth phase observations were obtained periods of more rapid field line stretching, thus reducing the total earthward electric drift. Since the magnetic field lines around midnight are mainly along the x-z plane, the above effects do not strongly affect V_y.

[30] Besides affecting the plasma transport, the strong diamagnetic drift also plays an important role in restraining the plasma sheet energization. Diamagnetic drift is the response to a pressure gradient, which in our simulation results from electric drift. It diverts plasma to a drift path along which the associated plasma energization is smaller than the path along the electric drift. At the same time, currents associated with particle's diamagnetic drift stretch magnetic field lines, which results in stronger magnetic force in balance with the enhanced plasma pressure force. The magnitude of the radial gradient of flux tube volume becomes smaller as field lines become more stretched, thus weakening the energization as plasma drifts earthward. These two negative feedbacks from diamagnetic drift and field line stretching restrain the energization of the plasma sheet as it drifts earthward.

3.4. Magnetic Field

[31] The equatorial magnetic field strengths along the midnight meridian for different $\Delta\Phi_{PC}$ are plotted in Figure 9. In general the field strengths decreases quickly from several 10s nT in the inner magnetosphere to less than 10 nT in the plasma sheet and then remains relatively constant with increasing distance from the Earth, resulting in a sharp radial gradient at the inner edge of the plasma sheet and a flat radial profile in the plasma sheet. The radial profiles show a slight local minimum at the inner edge of the plasma sheet, which is due to a strong peak in the current density at the inner edge of the plasma sheet that generates negative (positive) ΔB earthward (tailward) of the peak. As convection increases, the earthward extension of the plasma sheet causes a strong decrease in the magnetic field at $X_{GSM} \sim -6$ to $-10\ R_E$. The local minimum also moves earthward but the minimum strength remains almost the same. The field strengths in the region tailward of the local minimum increase slightly with activity but remain less than 10 nT.

[32] Figure 10a shows that these changes agree well with the Geotail magnetic field shown in Figure 9 in Paper 1. The change of the simulated B_z at $Z_{GSM} = 0$ at geosynchronous orbit also agrees with the changes in the largest B_z measured

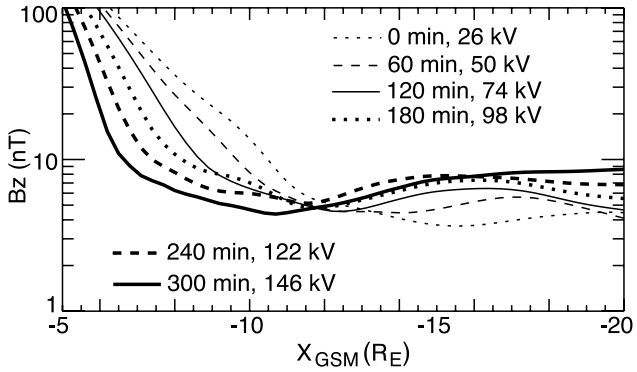

Figure 9. Radial profiles of the simulated B_z at midnight in the equatorial plane.

by geosynchronous satellites during the same quiet and growth phase periods observed by Geotail (since the geosynchronous satellites may not be near the current sheet, we plot the B_z data only when $|B_x| \leq 20$ nT. We expect the largest observed B_zs should be closer to the true B_z magnitudes in the equatorial plane). However, it is impossible to confirm the local minimum seen in the simulated radial profiles with measurements from a single spacecraft. Figures 10b and 10c shows the simulated B_x and B_z at $Z_{GSM} = 1.5\ R_E$, respectively, and their comparisons with the Geotail lobe magnetic field. We can see that the simulated B_x increases strongly at small radial distance with convection strength and that the changes are in reasonable agreement with the Geotail observations. The simulated B_z is

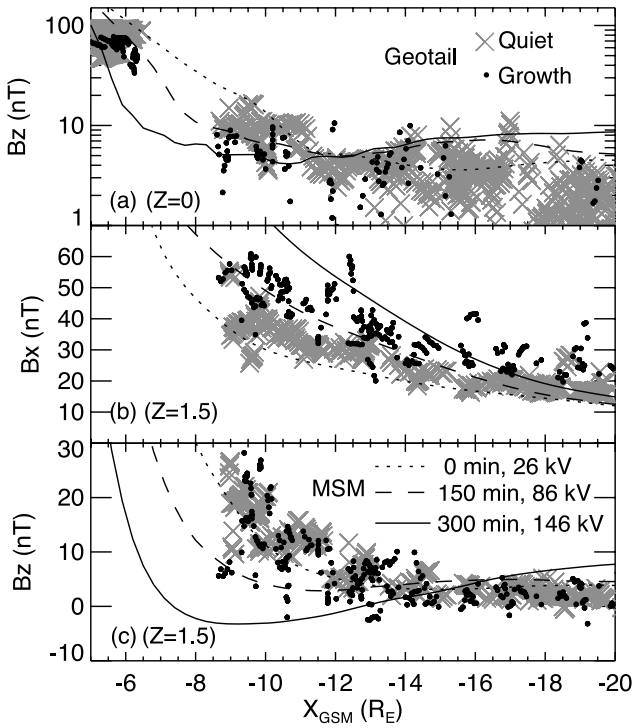

Figure 10. Comparisons of (a) the B_z in the equatorial plane, (b) the B_x in the lobes, and (c) the B_z in the lobes between the simulated magnetic field and the Geotail data shown in Figure 8 in Paper 1.

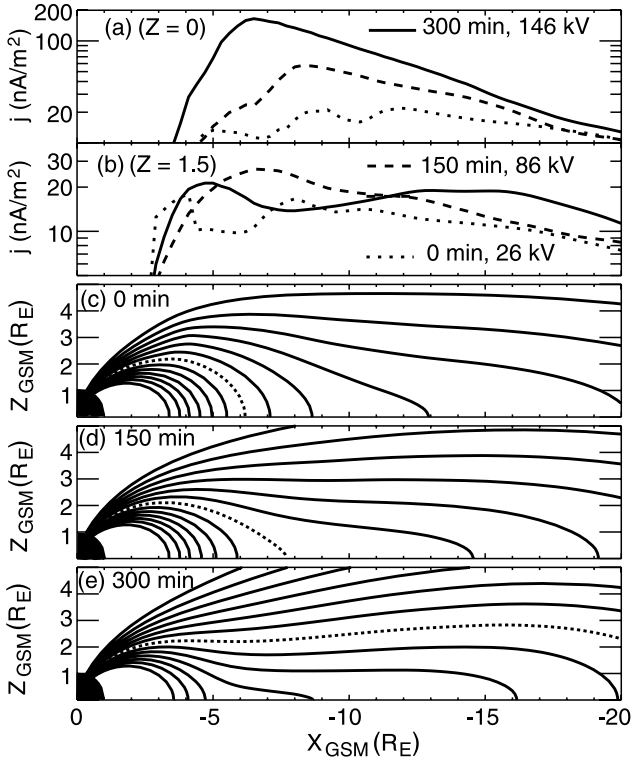

Figure 11. Radial profiles of the simulated current density at (a) $Z_{GSM} = 0$ and at (b) $Z_{GSM} = 1.5\ R_E$. The simulated magnetic field lines from fixed latitudes in the ionosphere at (c) $t = 0$ min, at (d) $t = 150$ min, and at (e) $t = 300$ min. The dotted lines in Figures 11c–11e correspond to field lines with the ionosphere footprint at 64.2° latitude.

seen to have little changes beyond $X_{GSM} \sim -14\ R_E$ as convection increases, consistent with the Geotail data. Earthward of $X_{GSM} \sim -14\ R_E$, the simulated B_z decreases as convection increases and the decrease is more significant at smaller radial distances. Even though the change seen in the Geotail B_z from quiet to growth phase conditions in the same region is not as clear as that seen in the simulated B_z, the smallest B_zs observed by Geotail during the growth phase are indeed lower than those observed during quiet times and the smallest B_z values observed for both conditions are in reasonable agreement with the simulated results. Therefore both our simulated pressure and force-balanced magnetic field are able to quantitatively reproduce the observed plasma sheet transition from weak to strong convection.

[33] Figures 11a and 11b show the radial profiles of current density along the midnight meridian at $Z_{GSM} = 0$ and 1.5 R_E, respectively. We find as convection increases, the half-thickness of the current sheet becomes smaller in the inner edge of the plasma sheet. Figure 11c shows magnetic field lines for different $\Delta\Phi_{PC}$ from the same latitude in the ionosphere. The field lines become more stretched and the region of stretched field lines moves earthward as convection increases because of the overall increase of plasma pressure in the plasma sheet and the earthward penetration of the plasma sheet as shown in Figure 2.

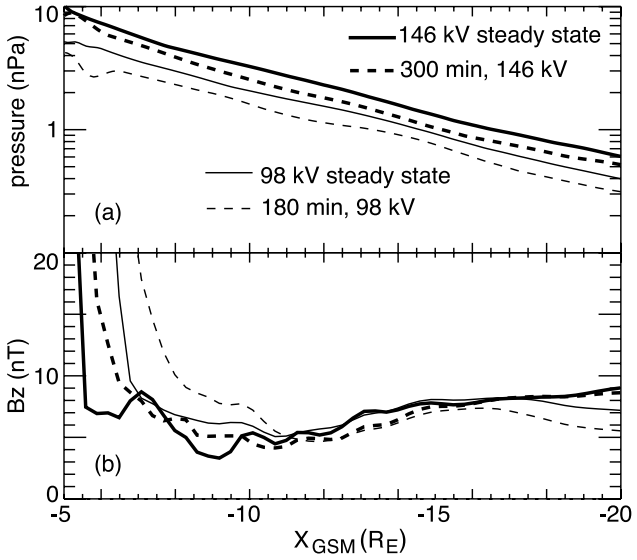

Figure 12. Comparisons in (a) the proton pressure averaged over $|Y_{GSM}| \leq 5\ R_E$ and (b) the B_z at midnight in the equatorial plane between the final steady states and the states at the time when convection is turning into constant.

[34] In the magnetotail, B_z becomes negative at higher latitudes. As field lines become more stretched, the region where B_z turns negative becomes closer to the equatorial plane. We find in our magnetic fields that the lowest position of the negative B_z at $X_{GSM} = -10\ R_E$ decreases from $Z_{GSM} \sim 5\ R_E$ for $\Delta\Phi_{PC} = 26$ kV to $Z_{GSM} \sim 3\ R_E$ for $\Delta\Phi_{PC} = 98$ kV. This decrease in Z_{GSM} can explain the Geotail observations shown in Figure 10 in Paper 1 that negative B_z in the lobe can be observed at smaller radial distance during the growth phase than during quiet times.

3.5. Steady State Plasma Sheet

[35] We have simulated the plasma sheet under weak convection and were able to obtain quiet time equilibrium [*Wang et al.*, 2001, 2002]. In order to see if the plasma and magnetic field can also reach a steady state under constant convection with moderate and strong strength, we run two simulations, one starting at $t = 180$ min under constant $\Delta\Phi_{PC} = 98$ kV and $\theta = 57.6°$ and another starting at $t = 300$ min under constant convection with $\Delta\Phi_{PC} = 146$ kV and $\theta = 51.8°$, after having run our simulation under steadily increasing convection to $t = 180$ min and 300 min. The changes after the convection becomes constant are relatively small. However, in both cases we find that the plasma sheet keeps moving earthward and pressure keeps increasing after the convection strength becomes constant due to the slow earthward drift of lower-energy particles. The changes gradually become smaller until there is no further change (after about 2 hours for both $\Delta\Phi_{PC} = 98$ kV and 146 kV), and both the pressure and magnetic field reach a steady state. Therefore our simulation shows that the plasma transport under strong and constant convection can result in a steady state plasma sheet. Figure 12 shows the comparisons of pressure and equatorial magnetic field strength of the two steady states and the profiles at the beginning of constant convection. The profiles are similar only with the profiles for the steady states being slightly closer to the Earth. The field minimums do not become smaller for the steady states.

[36] Not only do our steady state profiles confirm qualitatively the results from previous steady state modeling [*Hau et al.*, 1989; *Hau*, 1991; *Erickson*, 1992; *Toffoletto et al.*, 1996, 2001], our simulations provide quantitative and validated steady state profiles of the plasma pressure and magnetic field for convection strengths ranging from very weak to very strong. Also, our results indicate that the plasma sheet will not disrupted by force imbalance under steady convection as predicted by *Erickson and Wolf* [1980] if the effects of magnetic drift and force-balanced magnetic field, as discussed in 3.3, are taken into account. This thus provides a validated steady state solution for constant convection.

4. Discussion

4.1. Effect of the Shielding of Convection Electric Field and Penetration Electric Field

[37] To investigate the effect of the shielding of the convection electric field on the resulting plasma sheet under the same $\Delta\Phi_{PC}$, we compare in Figure 13 the results for $\Delta\Phi_{PC} = 98$ kV from the current simulation, where we lowered the shielding latitude correspondingly with $\Delta\Phi_{PC}$ ($\theta = 59°$ for $\Delta\Phi_{PC} = 98$ kV, corresponding to $r \sim 5\ R_E$ at midnight), with the results from our previous simulation [*Wang et al.*, 2003] where the shielding latitude was fixed at $\theta = 66.5°$ (corresponding to $r \sim 10\ R_E$ at midnight). The shielding redistributes the electric potential in the region adjacent to and outward of the shielding edge. As seen in Figure 13, at $X_{GSM} = -11\ R_E$ the electric field is smaller near midnight and larger near the flanks when the shielding is at $r \sim 10\ R_E$ than that when the shielding is at $r \sim 5\ R_E$ but the difference becomes very small at $X_{GSM} = -18\ R_E$. Since the convection electric field **E** is directed mainly toward positive Y as shown in Figure 13 and the y component of the current sheet current density **j** is largest at midnight but becomes small toward larger $|Y|$ at constant X, the electric field near midnight becoming stronger as the shielding moves earthward from $r \sim 10\ R_E$ to $r \sim 5\ R_E$ results in stronger particle energization $\mathbf{E}\cdot\mathbf{j}$ for the same $\Delta\Phi_{PC}$. This indicates that plasma sheet energization can be affected by both the solar wind condition ($\Delta\Phi_{PC}$) and by the ionosphere feedback that gives rise to shielding.

[38] Our assumption of no penetration electric field becomes inappropriate when convection increases more quickly than in this simulation, such as often happens during the storm main phase or the substorm growth phase after the IMF rapidly becomes significantly southward. This is because shielding is ineffective for ~30–60 min after a rapid increase in convection [*Garner*, 2003]. Geosynchronous observations near midnight local time during the substorm growth phase [*Birn et al.*, 1997] show that ion pressure ranges from 2 to 3 nPa, density ranges from 1.2 to 1.4 cm^{-3}, and temperature is between 9 to 13 keV. However, our results for these three ion moments for $\Delta\Phi_{PC} = 26$ to 86 kV and the shielding at $r \sim 10$ to 6 R_E (the range for which our results show good agreement with the Geotail growth phase observations) are smaller than the geosynchronous observations and can only reach the observed

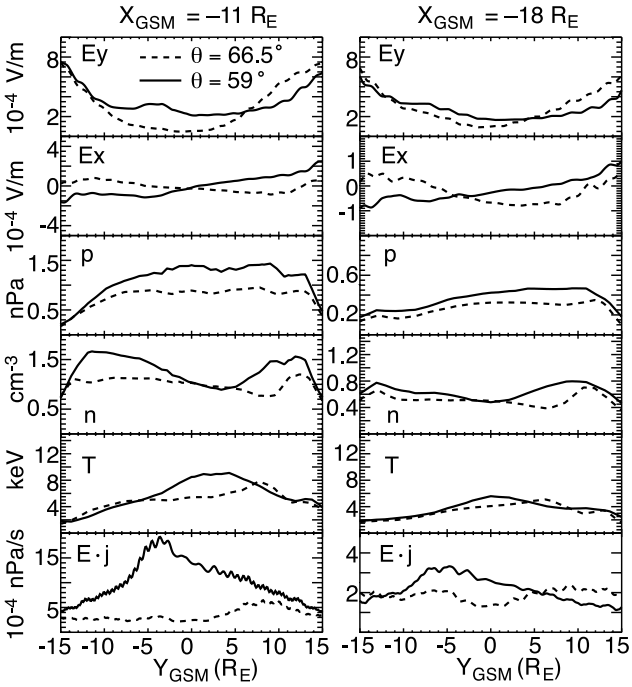

Figure 13. Comparisons of the cross-tail profiles at two X_{GSM} locations between simulation results with two different shielding latitudes for the same $\Delta\Phi_{PC}$ = 98 kV.

ranges when $\Delta\Phi_{PC} \geq 98$ kV and the shielding at $r \leq 6\ R_E$. In addition, Figure 2a shows that particles from the tail source result in a pressure peak of ~10 nPa at $r \sim 5\ R_E$ when $\Delta\Phi_{PC}$ = 146 kV and the shielding is at $r \sim 4\ R_E$. However, the storm time ring current is at $r \leq 4$ [*Smith and Hoffman*, 1973], which is closer to the Earth than the plasma sheet particles can reach in our simulation. These comparisons indicate that the convection electric field with efficient shielding can neither bring the plasma sheet to geosynchronous orbit under a typical $\Delta\Phi_{PC}$ range for the substorm growth phase nor to the region where the storm-time ring current forms under very high $\Delta\Phi_{PC}$. Thus the penetration electric field following a quick convection increase must play an important role in bringing particles to smaller geocentric radial distances.

4.2. Importance of the Hall Term in the Generalized Ohm's Law in the Plasma Sheet

[39] The generalized Ohm's law is

$$\mathbf{E} = -\mathbf{v}\times\mathbf{B} + \frac{1}{ne}\mathbf{j}\times\mathbf{B} + \eta\mathbf{j} - \frac{1}{ne}\nabla\cdot\mathbf{p}_e + \frac{m_e}{e^2 n}\left[\frac{\partial\mathbf{j}}{\partial t} + \nabla\cdot(\mathbf{jv} + \mathbf{vj})\right], \quad (5)$$

where η is resistivity and $\mathbf{p}_e$ is the electron pressure tensor [*Siscoe*, 1983]. For many regions of space plasma, the magnitudes of the two terms, $\mathbf{E}$ and $-\mathbf{v}\times\mathbf{B}$, are similar and much larger than other terms. This leads to the frozen-in condition, $\mathbf{E} = -\mathbf{v}\times\mathbf{B}$, used in ideal MHD. However, in the region of the plasma sheet where $\mathbf{j}$ is strong the magnitude of the Hall term may be comparable to $\mathbf{E}$ and should not be neglected. Therefore it may result in considerable error when ideal MHD is used to simulate the plasma sheet. We showed that this was the case in *Wang et al.* [2001, 2003] and we find that this is the case in the current simulation as well.

[40] Here we look at this lack of validity as it affects magnetic field changes using Faraday's law. Considering the plasma sheet in a steady and force balanced state, the momentum equation becomes $\mathbf{j}\times\mathbf{B} = \nabla p$, which requires plasma to have a charge-dependent diamagnetic drift to maintain a system's force balance. Since in the plasma sheet the electron pressure is ~7 times smaller than ion pressure in the plasma sheet and the electron density is similar to the ion density, the ion diamagnetic drift is stronger than the electron diamagnetic. Therefore the total drift $\mathbf{v} = (m_i\mathbf{v}_i + m_e\mathbf{v}_e)/(m_i + m_e) \sim \mathbf{v}_i = \mathbf{E}\times\mathbf{B}/B^2 - (\mathbf{B}\times\nabla p_i)/(neB^2)$ where $\mathbf{v}_i$ is ion drift, $\mathbf{v}_e$ is electron drift, m_i is ion mass, m_e is electron mass, and p_i is ion pressure. Therefore Faraday's law, when using the frozen-in condition, becomes $\partial\mathbf{B}/\partial t = -\nabla\times(\mathbf{v}\times\mathbf{B}) = \nabla\times(-\mathbf{E} + \nabla p_i/ne)$. In a steady state $\partial\mathbf{B}/\partial t = 0$ and $\nabla\times\mathbf{E} = -\nabla\times\nabla\phi = 0$. However, we investigate our steady state results for both $\Delta\Phi_{PC}$ = 98 and 146 kV and find that, as shown in Figure 14 for $\Delta\Phi_{PC}$ = 146 kV, the magnetic field change in 30 min due to $\nabla\times(\nabla p_i/ne)$ can be in the same order of magnitude as the background magnetic field itself. This is a nonnegligible error. Therefore it is necessary to keep the Hall term in the generalized Ohm's law, which will cancel out $\nabla p_i/ne$ in the Faraday's law under the condition of force balance, to obtain a correct description of magnetic field changes.

5. Summary

[41] We have used a modified version of the Magnetospheric Specification Model and a modified version of the Tsyganenko 96 model to simulate proton electric and magnetic drifts with two-dimensional force balance maintained along the midnight meridian and obtain proton distributions and magnetic fields within the plasma sheet. The strength of the model convection electric field is determined by the cross polar cap potential drop ($\Delta\Phi_{PC}$) and the field is shielded below a latitude θ. The local time–dependent proton differential fluxes assigned to the model boundary are a mixture of hot plasma from the deep tail and cooler plasma from the low-latitude boundary layer. We first simulated the plasma sheet under weak convection and

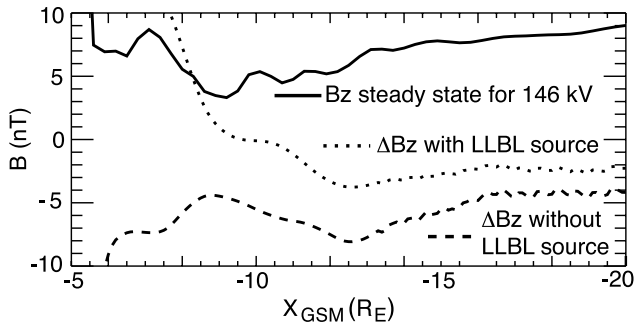

Figure 14. Comparisons of the simulated steady state B_z in the equatorial plane for $\Delta\Phi_{PC}$ = 146 kV and the estimated magnetic field change in 30 min (ΔB_z) due to $\nabla\times(\nabla p_i/ne)$ using results from the steady state for $\Delta\Phi_{PC}$ = 146 kV.

obtain two-dimensional quiet time equilibrium. We then increase convection steadily and slowly by increasing $\Delta\Phi_{PC}$ and lowering θ while keeping the boundary sources time-independent, thus obtaining a series of nearly steady state plasma sheet profiles for different strengths of convection. We compared the radial profiles of the simulated plasma moments and magnetic field with the Geotail observations presented in Paper 1 for weak and strong convection.

[42] The simulated proton pressure radial profiles and the change with convection strength agree well both qualitatively and quantitatively with the Geotail total pressures, indicating the energization associated with adiabatic electric and magnetic drift is sufficient to account for the observed pressure increase. The pressure is higher in the premidnight sector near the inner edge of the plasma sheet due to proton's duskward magnetic drift. Comparing with the Geotail data, our convection strength–independent LLBL source is too weak for quiet times but too strong for enhanced convection, which indicates the plasma sheet number density and temperature are strongly affected by particles originating from the LLBL during quiet times, but not during the growth phase.

[43] The simulated flows show the earthward electric drift is diverted toward dusk by proton's duskward diamagnetic drift regardless of convection strength, but the flow speed increases with increasing convection. These features are consistent with observations, revealing the importance of diamagnetic drift in plasma sheet dynamics.

[44] The simulated magnetic field shows a decrease in B_z and an increase in B_x in both the current sheet and lobe as convection increases, and field lines become more stretched during stronger convection. The radial magnetic field profiles and the changes with convection strength reproduce well the observations from Geotail and geosynchronous orbit satellites. The region where the lobe B_z turns negative due to magnetic field lines flaring outward becomes closer to the equatorial plane as convection increases and field lines become more stretched. This explains the observation that negative lobe B_z during the growth phase can be seen at smaller radial distance than during quiet times.

[45] We found the plasma sheet under strong and constant convection can become steady. The validity of our steady state profiles is supported by our model's ability to quantitatively predict the plasma sheet change from weak to strong convection. The results point out the effects of magnetic drift and force-balanced magnetic field in restraining plasma energization, thus bringing the plasma sheet away from the possible convection disruption due to force imbalance predicted by *Erickson and Wolf* [1980].

[46] With the same $\Delta\Phi_{pc}$ applied, the shielding of the convection electric field prevents the earthward motion of the plasma sheet and redistributes the electric potential so that the energization near the edge of shielding significantly decreases. Our results indicate the penetration electric field, which is important when convection increase is fast, should play an important role in bringing the plasma sheet particles to small radial distance during the growth phase of substorms, when $\Delta\Phi_{pc}$ may not be strong, and during the main phase of storms.

[47] Finally, we have found that strong diamagnetic drift in the plasma sheet may result in significant error in the magnetic field calculated from Faraday's law when using the frozen-in condition in the MHD equations. Analysis of our steady state results suggests that the error is too large to be neglected, and the Hall term must be included in the generalized Ohm's law in order to correct this error.

[48] **Acknowledgments.** This work has been supported at UCLA by NSF grant ATM- 0207298. The work by M. W. Chen has been supported by NSF grants ATM-0207160 and ATM-0202108. The work of M. W. Chen was also supported under the Aerospace Corporation's Independent Research and Development Program. The work by F. R. Toffoletto has been supported by the NASA SEC Theory Program under grant NSG5-11881. We wish to thank N. A. Tsyganenko for his assistance in making modifications to the Tsyganenko 96 magnetic field model. We thank R. A. Wolf for valuable discussion. We also wish to thank H. Singer at NOAA SEC and CDAWeb for the use of magnetic field data from geosynchronous orbit satellites.

[49] Arthur Richmond thanks the reviewer for their assistance in evaluating this paper.

References

Angelopoulos, V. (1996), The role of impulsive particle acceleration in magnetotail circulation, in *Proceedings of the Third International Conference on Substorms (ICS-3)*, *Spec. Publ. 389*, pp. 17–22, Eur. Space Agency, Noordwijk, Netherlands.

Angelopoulos, V., et al. (1993), Characteristics of ion flow in the quiet state of the inner plasma sheet, *Geophys. Res. Lett.*, *20*, 1711–1714.

Ashour-Abdalla, M., L. M. Zelenyi, V. Peroomian, and R. L. Richard (1994), Consequences of magnetotail ion dynamics, *J. Geophys. Res.*, *99*, 14,891–14,916.

Baumjohann, W., G. Paschmann, and G. A. Cattell (1989), Average plasma properties in the central plasma sheet, *J. Geophys. Res.*, *94*, 6597–6606.

Birn, J., M. F. Thomsen, J. E. Borovsky, G. D. Reeves, D. J. McComas, and R. D. Belian (1997), Characteristic plasma properties during dispersionless substorm injections at geosynchronous orbit, *J. Geophys. Res.*, *102*, 2309–2324.

Borovsky, J. E., M. F. Thomsen, and D. J. McComas (1997), The superdense plasma sheet: Plasmaspheric origin, solar wind origin, or ionospheric origin?, *J. Geophys. Res.*, *102*, 22,089–22,106.

Chen, M. W., M. Schulz, and L. R. Lyons (1994), Energy content of stormtime ring current from phase space mapping simulations, *Geophys. Res. Lett.*, *20*, 1727–1730.

Erickson, G. M. (1992), A quasi-static magnetospheric convection model in two dimensions, *J. Geophys. Res.*, *97*, 6505–6522.

Erickson, G. M., and R. A. Wolf (1980), Is steady convection possible in the Earth's magnetotail?, *Geophys. Res. Lett.*, *7*, 897–900.

Freeman, J. W., R. A. Wolf, R. W. Spiro, B. Hausman, B. Bales, R. Hilmer, A. Nagai, and R. Lambour (1993), Magnetospheric specification model development code documentation, scientific description, and software documentation, *Contract F19628-90-K-0012*, Rice Univ. for Air Force Geophys. Lab., Hanscom Air Force Base, Mass.

Fujimoto, M., T. Terasawa, and T. Mukai (1998), The low-latitude boundary layer in the tail-franks, in *New Perspectives on the Earth's Magnetotail*, *Geophys. Monogr. Ser.*, vol. 105, edited by A. Nishida, D. N. Baker, and S. W. H. Cowley, pp. 33–44, AGU, Washington, D. C.

Garner, T. W. (2003), Numerical experiments on the inner magnetosphere electric field, *J. Geophys. Res.*, *108*(A10), 1373, doi:10.1029/2003JA010039.

Gussenhoven, M. S., D. A. Hardy, and N. Heinemann (1983), Systematics of the equatorward diffuse auroral boundary, *J. Geophys. Res.*, *88*, 5692–5708.

Hau, L.-N. (1991), Effects of steady state adiabatic convection on the configuration of the near-Earth plasma sheet, 2, *J. Geophys. Res.*, *96*, 5591–5596.

Hau, L.-N., R. A. Wolf, G.-H. Voigt, and C. C. Wu (1989), Steady state magnetic field configurations for the Earth's magnetotail, *J. Geophys. Res.*, *94*, 1303–1316.

Heppner, J. P., and N. C. Maynard (1987), Empirical high-latitude electric field models, *J. Geophys. Res.*, *92*, 4467–4489.

Hori, T., K. Maezawa, Y. Saito, and T. Mukai (2000), Average profile of ion flow and convection electric field in the near-Earth plasma sheet, *Geophys. Res. Lett.*, *27*, 1623–1626.

Huang, C. Y., and L. A. Frank (1986), A statistical survey of the central plasma sheet: Implications for substorm models, *Geophys. Res. Lett.*, *13*, 652–655.

Huang, C. Y., and L. A. Frank (1994a), Magnitude of B_z in the neutral sheet of the magnetotail, *J. Geophys. Res.*, *99*, 73–82.

Huang, C. Y., and L. A. Frank (1994b), A statistical survey of the central plasma sheet, *J. Geophys. Res.*, *99*, 83–95.

Kistler, L. M., W. Baumjohann, T. Nagai, and E. Möbius (1993), Superposed epoch analysis of pressure and magnetic field configuration changes in the plasma sheet, *J. Geophys. Res.*, *98*, 9249–9258.

Korth, H., M. F. Thomsen, J. E. Borovsky, and D. J. McComas (1999), Plasma sheet access to geosynchronous orbit, *J. Geophys. Res.*, *104*, 25,047–25,061.

Kozyra, J. U., J. E. Borovsky, M. W. Chen, M.-C. Fok, and V. K. Jordanova (1998), Plasma sheet preconditioning, enhanced convection and ring current development, in *Substorms-4*, edited by S. Kokubun and Y. Kamide, pp. 755–760, Kluwer Acad., Norwell, Mass.

Miura, A. (1995), Kelvin-Helmholtz instability at the magnetopause: Computer simulations, in *Physics of the Magnetopause*, *Geophys. Monogr. Ser.*, vol. 90, edited by P. Song, B. U. O. Sonnerup, and M. F. Thomsen, pp. 285–291, AGU, Washington, D. C.

Mitchell, D. G., F. Kutchko, D. J. Williams, T. E. Eastman, L. A. Frank, and C. T. Russell (1987), An extended study of the low-latitude boundary layer on the dawn and dusk flanks of the magnetosphere, *J. Geophys. Res.*, *92*, 7394–7404.

Ogino, T., R. J. Walker, and M. Ashour-Abdalla (1992), A global magnetohydrodynamic simulation of the magnetosheath and magnetosphere when the interplanetary magnetic field is northward, *IEEE Trans. Plasma Sci.*, *20*, 817–828.

Paterson, W. R., L. A. Frank, S. Kokubun, and T. Yamamoto (1998), Geotail survey of ion flow in the plasma sheet: Observations between 10 and 50 R_E, *J. Geophys. Res.*, *103*, 11,811–11,825.

Samson, J. C., L. R. Lyons, P. T. Newell, F. Creutzberg, and B. Xu (1992), Proton aurora and substorm intensifications, *Geophys. Res. Lett.*, *19*, 2167–2170.

Siscoe, G. L. (1983), Solar system magnetohydrodynamics, in *Solar-Terrestrial Physics*, edited by R. L. Carovillano and J. M. Forbes, pp. 11–100, D. Reidel, Norwell, Mass.

Smith, P. H., and R. A. Hoffman (1973), Ring current particle distributions during the magnetic storms of December 16–18, *J. Geophys. Res.*, *78*, 4731–4737.

Spence, H. E., and M. G. Kivelson (1993), Contributions of the low-latitude boundary layer to the finite width magnetotail convection model, *J. Geophys. Res.*, *98*, 15,487–15,496.

Spence, H. E., M. G. Kivelson, R. J. Walker, and D. J. McComas (1989), Magnetospheric plasma pressures in the midnight meridian: Observations from 2.5 to 35 R_E, *J. Geophys. Res.*, *94*, 5264–5272.

Spiro, R. W., R. A. Wolf, and B. G. Fejer (1988), Penetration of high-latitude-electric-field effects to low latitudes during SUNDIAL 1984, *Ann. Geophys.*, *6*, 39–50.

Toffoletto, F. R., R. W. Spiro, R. A. Wolf, M. Hesse, and J. Birn (1996), Self-consistent modeling of inner magnetospheric convection, in *Proceedings of the Third International Conference on Substorms (ICS-3)*, *Spec. Publ. 389*, edited by E. J. Rolfe and B. Kaldeich, pp. 223–230, Eur. Space Agency, Noordwijk, Netherlands.

Toffoletto, F. R., R. W. Spiro, R. A. Wolf, M. Hesse, and J. Birn (2001), Modeling inner magnetospheric electrodynamics, in *Space Weather*, *Geophys. Monogr. Ser.*, vol. 125, edited by P. Song, H. J. Singer, and G. L. Sisco, pp. 265–272, AGU, Washington, D. C.

Tsyganenko, N. A. (1995), Modeling the Earth's magnetospheric magnetic field confined within a realistic magnetopause, *J. Geophys. Res.*, *100*, 5599–5612.

Tsyganenko, N. A. (1996), Effects of the solar wind conditions on the global magnetospheric configuration as deduced from data-based field models, in *Proceedings of the Third International Conference on Substorms (ICS-3)*, *Spec. Publ. 389*, pp. 181–185, Eur. Space Agency, Noordwijk, Netherlands.

Tsyganenko, N. A. (1998), Data-based models of the global geospace magnetic field: Challenges and prospects of the ISTP Era, in *Geospace Mass and Energy Flow: Results From the International Solar-Terrestrial Physics Program*, edited by J. L. Horwitz, D. L. Gallagher, and W. K. Peterson, pp. 371–382, AGU, Washington, D. C.

Walker, R. J., T. Ogino, J. R. Raeder, and M. Ashour-Abdalla (1993), A global magnetohydrodynamic simulation of the magnetosphere when the interplanetary magnetic field is southward: The onset of magnetotail reconnection, *J. Geophys. Res.*, *98*, 17,235–17,249.

Wang, C.-P., L. R. Lyons, M. W. Chen, and R. A. Wolf (2001), Modeling the quiet time inner plasma sheet protons, *J. Geophys. Res.*, *106*, 6161–6178.

Wang, C.-P., L. R. Lyons, M. W. Chen, and R. A. Wolf (2002), Two-dimensional quiet time equilibrium for the inner plasma sheet protons and magnetic field, *Geophys. Res. Lett.*, *29*(24), 2186, doi:10.1029/2001GL013984.

Wang, C.-P., L. R. Lyons, M. W. Chen, R. A. Wolf, and F. R. Toffoletto (2003), Modeling the inner plasma sheet protons and magnetic field under enhanced convection, *J. Geophys. Res.*, *108*(A2), 1074, doi:10.1029/2002JA009620.

Wang, C.-P., L. Lyons, T. Nagai, and J. C. Samson (2004), Midnight radial profiles of the quiet and growth-phase plasma sheet: The Geotail observations, *J. Geophys. Res.*, *109*, A12201, doi:10.1029/2004JA010590.

Weimer, D. R., J. R. Kan, and S.-I. Akasofu (1992), Variations of the polar cap potential measured during magnetospheric substorms, *J. Geophys. Res.*, *97*, 3945–3951.

Wing, S., and P. T. Newell (1998), Central plasma sheet ion properties as inferred from ionospheric observations, *J. Geophys. Res.*, *103*, 6785–6800.

Wolf, R. A. (1983), The quasi-static (slow-flow) region of the magnetosphere, in *Solar Terrestrial Physics*, edited by R. L. Carovillano and J. M. Forbes, pp. 303–368, D. Reidel, Norwell, Mass.

Zhu, X. (1993), Magnetospheric convection pattern and its implications, *J. Geophys. Res.*, *98*, 21,291–21,296.

M. W. Chen, Space Science Applications Laboratory, MS M2-260, The Aerospace Corporation, 2350 E. El Segundo Boulevard, Los Angeles, CA 90009-2957, USA. (margaret.w.chen@aero.org)

L. R. Lyons and C.-P. Wang, Department of Atmospheric and Oceanic Sciences, MS-727, University of California, 405 Hilgard Avenue, Los Angeles, CA 90095-1565, USA. (larry@atmos.ucla.edu; cat@atmos.ucla.edu)

F. R. Toffoletto, Department of Physics and Astronomy, MS 108, Rice University, 6100 Main Street, Houston, TX 77005, USA. (toffo@rice.edu)